Composite Structures 304 (2023) 116358

Contents lists available at ScienceDirect

Composite Structures

journal homepage: www.elsevier.com/locate/compstruct

Thermal buckling and post-buckling analyses of rotating Timoshenko microbeams reinforced with graphene platelet

Arameh Eyvazian [a,b,*], Chunwei Zhang [a,**], Mohammad Alkhedher [c], Sami Muhsen [d], Mohamed Abdelghany Elkotb [e,f]

[a] Multidisciplinary Center for Infrastructure Engineering, Shenyang University of Technology, China No. 111 Shenliao West Rd., Shenyang, 110870, China
[b] Department of Mechanical Engineering, Politecnico di Milano (Technical University), Via La Masa 1, 20156 Milan, Italy
[c] Mechanical and Industrial Engineering Department, Abu Dhabi University, Abu Dhabi, 59911, United Arab Emirates
[d] Air Conditioning and Refrigeration Techniques Engineering Department, Al-Mustaqbal University College, Babylon, Iraq
[e] Mechanical Engineering Department, College of Engineering, King Khalid University, Abha 61421, Saudi Arabia
[f] Mechanical Engineering Department, College of Engineering, Kafrelsheikh University 33516, Egypt

ARTICLE INFO

Keywords:
Rotating nanocomposite beams
Graphene platelet reinforcement
Thermal buckling
Post-buckling response

ABSTRACT

A comprehensive study is established to investigate on the thermal buckling instability and the subsequent post-critical deflection of a rotating nanocomposite microbeam reinforced with graphene platelet. The main scope of the current research is shedding light on the effectiveness of reinforcing a rotating microbeam with graphene platelet subjected to a constant temperature development. The Timoshenko beam theory comes along the von-Karman strain displacement relations to extract the governing equations of motion in accordance with the modified couple stress theory. The modified Halpin–Tsai micromechanical model is implemented to determine the practical elasticity modulus of the nanocomposite beam. The Ritz technique is accompanied by the Chebyshev orthonormal polynomial set to discretize the weak form of the nonlinear equations of motion. The Newton–Raphson technique is applied to the discretized static nonlinear equations of motion to compute the static deformation due to the centrifugal force. On the basis of two effective algorithms the nonlinear equations of motion are attacked to find out the critical buckling temperature change as well as the succeeding post-critical deflection. It is observed that adjoining the graphene phase in the form of an X-pattern promotes the static strength of a rotating microbeam against the buckling instability. However, in contrast, for stationary microbeams and microbeams that rotate with a velocity below a threshold speed adjoining the graphene platelet reinforcement in the form of an O-Pattern not only does not strengthen the microbeam but also weakens it against the buckling instability. Moreover, the buckling modeshape of rotating simply-clamped microbeams is more impressed by the graphene phase.

1. Introduction

From enormous spaceships to tiny microturbines rotating beams are a common piece. During their life cycle they may be subjected to a thermal ambient or even they work in a thermal environment. Furthermore, their applications may induce some certain support conditions which are not usual such as a clamped-free (CF) one. In this respect, we are establishing an exploration to examine a possible buckling instability of such structures and the associated post-critical deflection. On other hand, we believe that making use of advanced materials, specifically reinforcing a matrix with graphene platelet (GPL) improves thermo-elastic features of the matrix phase. In this regard, with the aim of illuminating the truth of such idea we examine the impression of reinforcing phase on the static instability of a rotating GPL microbeam. Accordingly, the buckling instability and the post-critical deflection of a rotating GPL micro beam in a thermal environment is addressed in this paper.

Zhu et al. [1] conducted an examination to investigate on the static treatment and free vibrations of composite plates reinforced with carbon nanotube (CNT). The small scale analysis of post-critical response of a Timoshenko microbeam composed of functionally graded material (FGM) encountering a thermal ambient was addressed by Ansari et al. [2]. An investigation on the small scale thermal static instability as well as the free vibrations of FGM nanobeams undergone a thermal ambient was organized by Ebrahimi and Salari [3]. The effect

* Corresponding author at: Department of Mechanical Engineering, Politecnico di Milano (Technical University), Via La Masa 1, 20156 Milan, Italy.
** Corresponding author.
E-mail addresses: arameh.eyvazian@polimi.it (A. Eyvazian), zhangchunwei@sut.edu.cn (C. Zhang).

https://doi.org/10.1016/j.compstruct.2022.116358
Received 30 July 2021; Received in revised form 30 September 2022; Accepted 7 October 2022
Available online 14 October 2022
0263-8223/

of material gradient exponent on the small scale vibration attributes of non-uniform FGM microbeams was studied by Shafiei et al. [4]. Ghadiri and Shafiei [5] developed an investigation for the sake of demonstrating the impact of different temperature divisions on the free vibration features of rotating FGM microbeams regarding various end supports. A comparison study between the two beam hypothesis models, so-called Euler–Bernoulli, and Timoshenko models, in terms of formulating and free vibration examination of rotating tapered FGM microbeams was arranged by Shefiei et al. [6]. Ilkhani and Hosseini-Hashemi [7] made an investigation on small scale free vibrations as well as static instability of rotating beams. Selim et al. [8] studied the free vibrations of nanocomposite plates reinforced with CNT (CNTRC plates) in a thermal environment in the framework of the third order shear deformation theory of Reddy. Mirjavadi et al. [9] examined the thermal buckling of imperfect FGM porous microbeams. The modified couple stress theory (MCST) was employed to incorporate the size dependency to the governing equations. An investigation on the buckling instability and free vibrations of FGM nanobeams subjected to temperature increment was accomplished by Mirjavadi et al. [10]. Sahmani and Aghdam [11] examined the buckling instability and the post-critical deflection of GPL plates in the framework of the nonlocal strain gradient theory. An analysis on the buckling instability and post-critical deflection of FG GPL plates in thermal ambient was addressed by Shen et al. [12]. The static instability and parametric resonance of GPL beams subjected to an increment in the ambient temperature were discussed by Wu et al. [13]. They declared that the dynamic instability region broadens as a consequence of an increase in the axial force as well as the temperature. Ghorbani Shenas et al. [14], and [15] arranged a study with the purpose of illustrating the effects of pre-twisting angle, and its rate, and material gradient exponent on the small scale thermal static instability and the post-critical response of rotating pre-twisted FGM microbeams. Yang et al. [16] examined the buckling instability and free vibrations of FG GPL porous plates employing the Chebyshev–Ritz scheme. They investigated on the influence of the porosity on the presented outcomes. An examination was established by Zhong et al. [17] to illuminate the impact of the dispersion pattern and the volume fraction of the CNT on the free vibrations of CNTRC plates. The free vibrations as well as static instability of FG GPL nanocomposite plates bonded with two piezoelectric facesheets was examined by Lin et al. [18]. Eyvazian et al. [19] explored the influence of quasi-static compressive force on the buckling instability of a foam-core composite sandwich column. They indicated that the maximum critical load is associated to a specimen with Dyneema fabrics facesheets and aluminum plates. The free vibration analysis of damped viscoelastic sandwich GPL plates with a magnetorheological fluid core layer was performed by Eyvazian et al. [20]. The variations of the natural frequencies and the corresponding loss factors in terms of the GPL distribution pattern were demonstrated. Mao and Zhang [21] studied the electro-mechanical buckling instability and the post-critical deflection of FG GPL piezoelectric plates. The dynamic response of GPL cylindrical shells subjected to a moving harmonic load was examined by Eyvazian et al. [22]. The size dependency was included to the developed formulation by means of the nonlocal strain gradient theory. An investigation on the dynamic instability of a Timoshenko double-beam subjected to a compressive load was accomplished by Zhao et al. [23]. The thermoelastic forced vibration analysis of MEMS/NEMS was investigated by Zhao et al. [24] by means of an analytical approach in regard of Green's functions.

Arvin [25] examined the dynamic instability of rotating CF isotropic beams subjected to a principal parametric resonance as a consequence of varying rotational velocity. The impacts of damping ratio, and the rotational velocity on the instability region were illuminated. The buckling instability of rotating CNTRC beams subjected to a temperature increment was studied by Khosravi et al. [26]. The impression of the dispersion type of the CNT on the buckling modeshape and the critical temperature was demonstrated. Khosravi et al. [27] investigated on the natural frequencies and the corresponding modeshapes of rotating CNTRC beams. The finite element method (FEM) was employed by Hosseini et al. [28] to examine the critical temperature and the post-buckling transverse displacement of rotating FGM Euler–Bernoulli micro-beams modeled in the framework of the MCST. Hosseini et al. [29] studied on the fundamental natural frequency of rotating FGM Euler–Bernoulli microbeams before the buckling incidence and after it. Xu et al. [30] addressed the thermal static instability and the post-critical response of rotating CNTRC beams.

In this paper, for the first time we address the buckling instability and the post-critical deflection of rotating GPL microbeams in thermal ambient. Beside some numerical illustrations we want to elucidate whether the GPL phase always promotes the strength of rotating GPL microbeams against the static instability or not. According to the hypothesis of the Timoshenko beam theory in accompanied by the MCST the nonlinear motion equations are developed resorting to the von-Karman strain relations. Effective elasticity modulus of the rotating GPL beam is defined according to the Halpin–Tsai micromechanical model (Ref. [13]). Via the Ritz scheme in regard of the Chebyshev polynomial set the motion equations are discretized. By means of introduced qualified algorithms the static deformation induced as a result of the rotation, the buckling instability temperature, and the afterwards deflection are computed. The impacts of the GPL weight fraction, the GPL distribution type, the slenderness ratio, and the rotational velocity on the current outcomes are elucidated.

2. Deriving the motion equations

Fig. 1-*a* illustrates a rotating immovable clamped–clamped (CC) GPL nanocomposite beam (GPLRC beam) with length L. The rotating GPLRC beam is attached to a hub with radius R. The cross section of the rotating GPLRC beam is shown in Fig. 1-*b*, and -*c* with height h, and width b. The depicted GPL dispersion types are, respectively, X-pattern, and O-Pattern. The origin of a rotating frame is denoted by O. It is situated at the area center of a cross section of the beam bonded to the hub. The rotating frame rotates at speed ω_R identical to the rotational velocity of the hub. s-axis is oriented along the beam span, y-axis is directed along the beam width, and z-axis is toward the beam height.

The longitudinal and flexural displacements of a material particle situated at (s, y, z) are, respectively, defined by (Ref. [31]):

$$u = \bar{u}(s) + z\psi(s)$$
$$w = \bar{w}(s) \tag{1}$$

where $\bar{w}(s)$ is the flexural displacement for a material particle located at the area center of the beam cross section at s, $\bar{u}(s)$ is its longitudinal displacement, and $\psi(s)$ is the flexural rotation of the mentioned cross section.

In accordance with the von-Karman hypotheses for strains and rotations (Ref. [31]), the normal and shear strains, respectively, hold as:

$$\varepsilon_{ss} = \partial_s u + \frac{1}{2}[\partial_s w]^2, \tag{2}$$

and

$$\gamma_{sz} = \partial_z u + \partial_s w \tag{3}$$

where ε_{ss} stands for the normal strain, and γ_{sz} denotes the shear strain. Furthermore, ∂ represents the derivative of the upcoming variable with respect to its subscript.

From Eq. (1) the longitudinal and flexural displacements are put into the given relations for the normal and shear strains, i.e. Eqs. (2), and (3). The ensuing relations, respectively, read:

$$\varepsilon_{ss} = \varepsilon^{(0)}(s) + z\kappa(s) \tag{4}$$

and

$$\gamma_{sz} = \psi(s) + \partial_s\bar{w}(s) \tag{5}$$

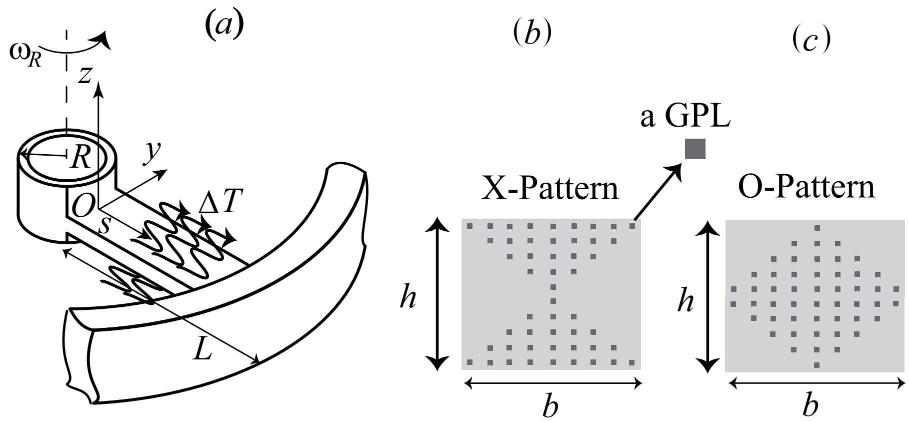

Fig. 1. (*a*)- A rotating CC GPLRC beam; A cross section of the GPLRC beam with (*b*)- X-pattern of GPLs, and (*c*)- O-pattern of GPLs.

where

$$\varepsilon^{(0)} = \partial_s \bar{u}(s) + \frac{1}{2}\partial_s \bar{w}(s)^2, \tag{6}$$

and

$$\kappa = \partial_s \psi(s). \tag{7}$$

Regarding the assumption of linear elasticity the constitutive relations for the kth GPL lamina subjected to a temperature change, i.e. ΔT, read (Ref. [31]):

$$\sigma_{ss}^{[k]} = Q_{11}^{[k]}[\varepsilon^{(0)}(s) + z\kappa(s) - \alpha^{[k]}\Delta T], \tag{8}$$

and

$$\tau_{sz}^{[k]} = Q_{55}^{[k]}\gamma_{sz} \tag{9}$$

where $\Delta T \equiv T - T_0$ in which T is the current temperature while T_0 is the reference temperature. $Q_{11}^{[k]} = E^{[k]}/(1-\nu^{[k]2})$ is the reduced stiffness of the kth GPL lamina wherein $E^{[k]}$ is the corresponding elasticity modulus, and $\nu^{[k]}$ is the associated Poisson's constant. $Q_{55}^{[k]} = G^{[k]}$ is the reduced shear stiffness of the kth GPL lamina wherein $G^{[k]}$ is the corresponding shear modulus. Moreover, $\alpha^{[k]}$ is the thermal expansion constant of the kth GPL lamina.

The MCST (Ref. [28]) is employed to incorporate the size dependency into the developed formulation for the rotating GPLRC microbeam. Accordingly, the deviatoric part of the couple stress moment of the kth GPL lamina, $m_{xy}^{[k]}$, is defined by (Ref. [28]):

$$m_{xy}^{[k]} = 2G^{[k]}l^{[k]2}\chi_{xy} \tag{10}$$

where $l^{[k]}$ is the material length scale parameter of the kth GPL lamina. Moreover, χ_{xy} is the symmetric curvature determined by (Ref. [28]):

$$\chi_{xy} = 1/2(\partial_y\theta_x + \partial_x\theta_y) \tag{11}$$

wherein $\boldsymbol{\theta}$ is the rotation vector described by (Ref. [28]):

$$\boldsymbol{\theta} = \frac{1}{2}(\nabla \times \mathbf{F}) \tag{12}$$

in which ∇ is the gradient vector. $\mathbf{F}$ is the displacement field vector reads:

$$\mathbf{F} = [u \quad 0 \quad w]. \tag{13}$$

The replacement of the displacement field vector into the rotation vector releases the nonzero component of the rotation vector:

$$\theta_y = \frac{1}{2}\psi(s) - \frac{1}{2}\partial_s\bar{w}(s) \tag{14}$$

The substitution of the rotation vector component into the symmetric curvature, i.e. Eq. (11), reshuffles χ_{xy} into:

$$\chi_{xy} = \frac{1}{4}\partial_s\psi(s) - \frac{1}{4}\partial_{ss}\bar{w}(s). \tag{15}$$

Table 1
The GPL volume fraction of the kth GPL lamina according to the GPL distribution pattern of a GPL laminate (Ref. [13]).

Pattern	V_{CN}
X	$V_{GPL}^{[k]} = 2V_{GPL}^{*}\lvert 2k - N_L - 1\rvert/N_L$
O	$V_{GPL}^{[k]} = 2V_{GPL}^{*}(1 - \lvert 2k - N_L - 1\rvert/N_L)$

2.1. Effective thermo-elastic constants for a GPL lamina

With the purpose of estimating the effective thermo-elastic constants for a GPL lamina, the modified Halpin–Tsai micromechanical model (Ref. [13]) is employed. Assume that the GPL volume fraction of the kth GPL lamina is $V_{GPL}^{[k]}$. In this respect, the corresponding elasticity modulus is specified by (Ref. [13]):

$$E^{[k]} = \frac{3}{8}\frac{1+\xi_a\eta_a V_{GPL}^{[k]}}{1-\eta_a V_{GPL}^{[k]}}E_m + \frac{5}{8}\frac{1+\xi_b\eta_b V_{GPL}^{[k]}}{1-\eta_b V_{GPL}^{[k]}}E_m \tag{16}$$

where $\xi_a = 2\frac{a_{GPL}}{t_{GPL}}$, and $\xi_b = 2\frac{b_{GPL}}{t_{GPL}}$ are the geometrical aspect ratios for a GPL. Moreover, η_b and η_a are defined, respectively, by (Ref. [13]):

$$\eta_a = \frac{E_{GPL}/E_m - 1}{E_{GPL}/E_m + \xi_a},$$
$$\eta_b = \frac{E_{GPL}/E_m - 1}{E_{GPL}/E_m + \xi_b} \tag{17}$$

The GPL volume fraction of the kth GPL lamina is specified in line with the GPL distribution pattern of a GPL laminate. The associated relations are released in Table 1: where hereafter, the GPL, and m subscripts stand for an attribute associated to the GPL and the matrix phases, respectively. N_L is the number of GPL laminas in the GPL laminate. Moreover, $V_{GPL}^{*} = \frac{W_{GPL}}{W_{GPL}+(\rho_{GPL}/\rho_m)(1-W_{GPL})}$ is the total GPL volume fraction of the GPL laminate in which W_{GPL} is the total GPL weight fraction of the GPL laminate, and ρ_{GPL}, and ρ_m are the mass densities, respectively, associated to the GPL and the matrix phases.

The mass density, the Poisson's coefficient and the thermal expansion constant of the kth GPL lamina are specified, respectively, according to (Ref. [13]):

$$\rho^{[k]} = V_{GPL}^{[k]}\rho_{GPL} + V_m^{[k]}\rho_m$$
$$\nu^{[k]} = V_{GPL}^{[k]}\nu_{GPL} + V_m^{[k]}\nu_m, \tag{18}$$

and

$$\alpha^{[k]} = V_{GPL}^{[k]}\alpha_{GPL} + V_m^{[k]}\alpha_m \tag{19}$$

where $V_m^{[k]} = 1 - V_{GPL}^{[k]}$ is the volume fraction of the matrix phase of the kth GPL lamina.

2.2. Action minimization

For the sake of deriving the motion equations, the principle of the stationary action (Ref. [32]), $\delta S = \int_{t_1}^{t_2}(\delta L)\mathrm{d}t = \int_{t_1}^{t_2}(\delta K - \delta U)\mathrm{d}t = 0$ between two arbitrary instants, i.e. t_1, and t_1, is employed. In the aforementioned relation, K is the kinetic energy of the system while U is its strain energy. According to this principle, among the all possible trajectories that are possible mathematically between the two arbitrary times, the one which for the action is minimized occurs practically.

The virtual strain energy is defined by (Refs. [28,31]):

$$\delta U = \int_0^L \int_{-\frac{1}{2}h}^{\frac{1}{2}h} [\sigma_{ss}\delta\varepsilon_{ss}(s) + \tau_{sz}\delta\gamma_{sz} + 2m_{xy}\delta\chi_{xy}]\mathrm{d}z\mathrm{d}s$$
$$\int_0^L \int_{-\frac{1}{2}h}^{\frac{1}{2}h} [\sigma_{ss}\{\delta\varepsilon^{(0)}(s) + z\delta\kappa(s)\} + \tau_{sz}\{\delta\gamma_{sz} + 2m_{xy}\delta\chi_{xy}\}]\mathrm{d}z\mathrm{d}s \tag{20}$$

By taking an integration over the beam height we have:

$$\delta U = \int_0^L [N_{ss}\delta\varepsilon^{(0)}(s) + M_{ss}\delta\kappa(s) + Q_{sz}\delta\gamma_{sz}^{(0)} + 2S_{xy}\delta\chi_{xy}]\mathrm{d}s \tag{21}$$

where N_{ss}, Q_{sz}, M_{ss}, and S_{xy}, are the stress, and couple stress resultants, respectively, defined by:

$$N_{ss} = -N_{ss}^T + A_{11}\varepsilon^{(0)}(s) + B_{11}\kappa(s), \tag{22}$$

$$Q_{sz} = A_{55}\gamma_{sz}(s), \tag{23}$$

$$M_{ss} = -M_{ss}^T + B_{11}\varepsilon^{(0)}(s) + D_{11}\kappa(s), \tag{24}$$

and

$$S_{xy} = A_{xy}\chi_{xy} \tag{25}$$

wherein N_{ss}^T, and M_{ss}^T, are, respectively, the thermal force and moment resultants while A_{ii}, $i = 1, 5$, B_{11}, and D_{11} are the longitudinal, flexural–longitudinal, and flexural elastic constants. Moreover, A_{xy} is the elastic constant relative to the size dependency of the microbeam. All the aforementioned parameters and constants are defined in Appendix.

The substitution of the above-mentioned parameters into the virtual strain energy leads to:

$$\begin{aligned}\delta U = \int_0^L [\{ & -N_{ss}^T + A_{11}\{\partial_s\bar{u}(s) + \frac{1}{2}\partial_s\bar{w}(s)^2\} \\ & + B_{11}\{\partial_s\psi(s)\}\}\delta\{\partial_s\bar{u}(s) + \frac{1}{2}\partial_s\bar{w}(s)^2\} \\ & + \{-M_{ss}^T + B_{11}\{\partial_s\bar{u}(s) + \frac{1}{2}\partial_s\bar{w}(s)^2\} + D_{11}\{\partial_s\psi(s)\}\}\delta\{\partial_s\psi(s)\} \\ & + \{A_{55}\{\psi(s) + \partial_s\bar{w}(s)\}\}\delta\{\psi(s) + \partial_s\bar{w}(s)\} + 2A_{xy}\chi_{xy}\delta\chi_{xy}]\mathrm{d}s\end{aligned} \tag{26}$$

The kinetic energy of a rotating GPL microbeam as a consequence of a rigid body rotation is determined according to (Ref. [28]):

$$K = \frac{1}{2}\int_0^L \int_{-\frac{1}{2}h}^{\frac{1}{2}h} \rho(z)[\omega_R^2(R + s + u)^2]\mathrm{d}z\mathrm{d}s \tag{27}$$

By substituting Eq. (1) into the kinetic energy relation and taking an integration over the height of the beam, we have:

$$K = \int_0^L \{\frac{1}{2}I_2\omega_R^2\psi(x,t)^2 + I_1\omega_R^2\psi(s)[R+x+\bar{u}(s)] + \frac{1}{2}I_0\omega_R^2[R+x+\bar{u}(s)]^2\}\mathrm{d}s \tag{28}$$

where the inertial terms, i.e. I_i $i = 0$ to 2, are specified in Appendix.

2.3. The Ritz route

To treat the nonlinear motion equations the Ritz scheme is implemented. One of the beneficial attributes of the Ritz scheme is its ability to attack directly the weak form of the motion equations. In this respect, the flexural displacement, the flexural rotation, and the longitudinal displacement, sequently, hold as (Ref. [33]):

$$\begin{aligned}\bar{w}(s) &= \Sigma_{i=0}^{\infty}[A_i\varphi_i^{(w)}(s)] \\ \psi(s) &= \Sigma_{m=0}^{\infty}[B_m\varphi_m^{(\psi)}(s)] \\ \bar{u}(s) &= \Sigma_{r=0}^{\infty}[C_r\varphi_r^{(u)}(s)]\end{aligned} \tag{29}$$

where A_i, B_m, and C_r, are the unknown Ritz coefficients, and $\varphi(s)$ is a space dependent term. The space dependent term should be separated into two multiplied terms, i.e. $\varphi_\alpha^{w,\psi,u}(s) = T_\alpha(s)R^{w,\psi,u}(s)$; The latter, i.e. $R^{w,\psi,u}(s)$, satisfies the geometric support conditions, while the former i.e. $T_\alpha(s)$, should be appointed from an orthonormal set (Ref. [33]). In this respect, the Chebyshev polynomial orthonormal set is assigned (Ref. [34]). The elements of the Chebyshev polynomial set, i.e. $T_i(s)$, are defined according to a recursive relation (Ref. [34]):

$$T_0(s) = 1, T_1(s) = 2\frac{s}{L} - 1, T_i(s) = 2(2\frac{s}{L} - 1)T_{i-1}(s) - T_{i-2}(s), \quad i = 2, 3, \ldots \tag{30}$$

Another part of the space dependent term that meets the geometric support conditions is specified as a polynomial function, i.e. $R^{w,\psi,u}(s) = (\frac{s}{L})^i(1-\frac{s}{L})^j$ (Ref. [35]), where i, and j can be 0 or 1 according to a given geometric support condition. For instance, for a simply-clamped (SC) support condition, the corresponding terms that fulfills the geometric support conditions, read:

$$R^w(s) = (\frac{s}{L})(1 - \frac{s}{L}), \quad R^\psi(s) = (1 - \frac{s}{L}), \quad R^u(s) = (\frac{s}{L})(1 - \frac{s}{L}) \tag{31}$$

Subsequently, the introduced separated form of the displacements, i.e. Eq. (29), along with the principle of stationary action, leads to:

$$\frac{\partial}{\partial A_i}\delta S = 0, \quad \frac{\partial}{\partial B_m}\delta S = 0, \quad \frac{\partial}{\partial C_r}\delta S = 0 \tag{32}$$

The expanded form for Eq. (32) reads:

$$\begin{aligned}&\{[\mathbf{K}][\mathbf{q},\mathbf{q}] - \omega_R^2[\mathbf{K}]^{\text{rotation}} - N_{ss}^T[\mathbf{K}]^{\text{thermal}}\}[\mathbf{q}] \\ &= \omega_R^2[\mathbf{F}]^{\text{rotation}} + N_{ss}^T[\mathbf{F}]^{\text{NT}} + M_{ss}^T[\mathbf{F}]^{\text{MT}} + R_{ss}^T[\mathbf{F}]^{\text{RT}}\end{aligned} \tag{33}$$

where $\alpha[\mathbf{F}]^\beta$ stands for the force vectors induced by the centrifugal and thermal forces. $[\mathbf{q}] = [\mathbf{A}, \quad \mathbf{B}, \quad \mathbf{C}]^T$ is the Ritz constants vector, and $[\mathbf{K}][\mathbf{q},\mathbf{q}][\mathbf{q}]$ is the third order nonlinear stiffness matrix.

2.4. Efficient proposed algorithms

For the sake of extracting the outcomes three developing steps are proposed. The first stage declares how the static deformation can be achieved as a consequence of centrifugal force, i.e. $\mathbf{q}_s$. The second step demonstrates how we can access to the buckling temperature. The last stage defines the determination of the post-critical deflection after the buckling instability incidence.

With the aim of determining static deformation as a result of centrifugal force, at a given temperature for a specified rotational velocity, the linearized form of Eq. (33) is solved. The obtained static deformation is used to extract the updated static deformation by means of the Newton–Raphson scheme (Ref. [31]). The route is continued until reaching a desired precision.

For the purpose of finding the critical temperature, the nonlinear buckling equation is linearized about the static deformation, i.e. $\{[\mathbf{K}][\mathbf{q}_s,\mathbf{q}_s] - \omega_R^2[\mathbf{K}]^{\text{rotation}} - N_{ss}^T[\mathbf{K}]^{\text{thermal}}\}[\mathbf{q}] = \mathbf{0}$. At first step the ensuing linearized buckling equation which is a standard eigenproblem,
i.e. $\{[\mathbf{K}][\mathbf{q}_s,\mathbf{q}_s] - \omega_R^2[\mathbf{K}]^{\text{rotation}}\}[\mathbf{q}] = N_{ss}^T[\mathbf{K}]^{\text{thermal}}[\mathbf{q}]$, is implemented to deliver the first approximation for the buckling temperature. All the thermoelastic features are defined in the updated critical temperature. The static deformation for the current critical temperature is obtained by the Newton–Raphson scheme. The process is iterated until accessing to the desired precision for the eigen-value of the buckling problem

Table 2
P_i coefficients for the modulus of elasticity, thermal expansion constant, the Poisson's constant, and the mass density of $SUS304$, and Si_3N_4 (Ref. [36]).

Material	P	P_0	P_{-1}	P_1	P_2	P_3
$SUS304$	E[Pa]	$201.04e9$	0	$3.079e-4$	$-6.534e-7$	0
	α $[\frac{1}{K}]$	$12.33e-6$	0	$8.086e-4$	0	0
	ν	0.28	0	0	0	0
	ρ [kg/m^3]	8166	0	0	0	0
Si_3N_4	E[Pa]	$348.43e9$	0	$-3.07e-4$	$2.16e-7$	$-8.946e-11$
	α $[\frac{1}{K}]$	$5.8723e-6$	0	$9.095e-4$	0	0
	ν	0.28	0	0	0	0
	ρ [kg/m^3]	2170	0	0	0	0

which is the thermal buckling temperature alongside its corresponding eigen-vector.

For the sake of determining the post-critical deflection after the buckling incidence, the nonlinear buckling equation about the static deformation, i.e. $\{[\mathbf{K}][\mathbf{q},\mathbf{q}]+[\mathbf{K}][\mathbf{q}_s,\mathbf{q}]+[\mathbf{K}][\mathbf{q}_s,\mathbf{q}_s]-\omega_R^2[\mathbf{K}]^{\text{rotation}}\}[\mathbf{q}] = N_{ss}^T[\mathbf{K}]^{\text{thermal}}[\mathbf{q}]$, is employed. At the first step the mid-point of the rotating GPLRC microbeam at position $(L/2,0,0)$ is appointed as the observing point. A final desired value for the deflection of the observing point is assumed, i.e. w_{mid}^{max}. Resorting to an assumed step size, the interval between the maximum deflection of the observing point and the minimum deflection which is zero is deviled into some sections to have smooth post-critical deflection curves. At the first stage the deflection of the observing point is considered equal to the assumed step size. The achieved eigen-vector in the buckling stage is rescaled, i.e. $\mathbf{q}_p$, in order to have a deformation equal to the current assumed deflection for the observing point. Thereafter, the nonlinear buckling equation is defined which is $\{[\mathbf{K}][\mathbf{q}_p,\mathbf{q}_p] + [\mathbf{K}][\mathbf{q}_s,\mathbf{q}_p] + [\mathbf{K}][\mathbf{q}_s,\mathbf{q}_s] - \omega_R^2[\mathbf{K}]^{\text{rotation}}\}[\mathbf{q}] = N_{ss}^T[\mathbf{K}]^{\text{thermal}}[\mathbf{q}]$. The associated eigen-problem delivers the critical post-critical temperature along with its eigen-vector. The procedure is resumed until we reach our desired precision at the assumed deflection for the observing point. Subsequently, the deflection of the observing point is updated by the step size. Thereafter, the process is executed for the new deflection until we reach the maximum assumed deflection for the observing point.

3. Discussion and results

In this section, we address the present numerical analysis in line with the introduced scopes of the research and the subsequent implications. Before we start, the developed formulation is verified. In this respect, the thermal buckling point of a stationary CC FGM beam (Ref. [36]) is examined. The slenderness ratio is $\eta = \frac{L}{h} = 25$, and the microbeam material length scale constant to the height proportion is 0.25. The metal phase, i.e. m-phase, is stainless steel 304, i.e. $SUS304$ and the ceramic phase, i.e. c-phase, is silicon-nitride, i.e. Si_3N_4. The associated material properties are temperature dependent. They are determined by means of $P = P_0 + P_1\left(\frac{T}{T_0}\right) + P_2\left(\frac{T}{T_0}\right)^2 + P_3\left(\frac{T}{T_0}\right)^3 + P_4\left(\frac{T}{T_0}\right)^4$ where T_0 is the reference temperature equal to 300 K, while T is the real-time temperature. The P_i coefficients for the modulus of elasticity, thermal expansion constant, the Poisson's constant, and the mass density, are mentioned in Table 2. The volume fraction of the ceramic phase is defined by $V_f = (1/2+z/h)^n$ in which n is the power law exponent. The elasticity modulus of the FGM microbeam is determined according to $E(z) = (E_c - E_m)V_f + E_m$. The present buckling temperature increments versus the associated values from Ref. [36] for $n = 0$, and $n = 1$ are represented in Table 3. Comparing the both elucidates the precision of the present developed formulation.

The other validation has been adjusted for the determination of the post-buckling response of a rotating CC symmetric sandwich FGM Euler–Bernoulli beam (Ref. [37]). The host lamina is made of a metal material namely $SUS304$. The facesheets are FGM. The FGM composed of a linear distribution of $SUS304$ as its metal state, and Si_3N_4 as its ceramic state. The FGM material attributes had been provided earlier in Table 2. The facesheets bonded to the host lamina at their metal phase surface. The beam rotates at $\omega_R^* \equiv \omega_R L\sqrt{\frac{\rho_m}{E_m^300}} = 0.15$ in which E_m^300 denotes the elasticity modulus of the metal phase specified in 300 K. The rotor radius to the length of the FGM sandwich beam ratio is 0.1. The bottom, and the top facesheets thicknesses are equal given by $h_b = h_t = \frac{1}{8}h_c$ where h_c denotes the host lamina thickness. The post-buckling curves are provided in terms of the dimensionless deflection of the mid-point of the sandwich beam, i.e. w_{obs}/h_c, in Fig. 2 for two beam slenderness ratios, i.e. $\eta \equiv L/h = 30$, and $\eta = 40$, where h stands for the total thickness of the sandwich beam. The results indicate that the outcomes match with a high accuracy.

Table 3
The present buckling temperature increments for an FGM stationary Timoshenko beam versus the associated values from Ref. [36].

The power law exponent	Current examination	Results of Ref. [36]
$n = 0$	619.1180	618.74
$n = 1$	454.3356	453.88

Moving forward some case studies reveal the impression of the material length scale parameter, the slenderness ratio, the rotational velocity, the GPL weight fraction, and the GPL dispersion type on the buckling temperature and the post-critical response outcomes. All the material properties are taken from Ref. [13] as follows; The matrix phase is epoxy; its elasticity modulus is 3.0 Gpa, its Poisson's constant is 0.34, its mass density is 1200 kg/m^3, and its thermal expansion constant is 60×10^{-6} 1/K. The GPL elasticity modulus is 1080 Gpa, its Poisson's constant is 0.186, its mass density is 1062.5 kg/m^3, and its thermal expansion constant is 5.0×10^{-6} 1/K. The weight fraction of the GPL is 0.3%. The height of the beam is $h^{ref} = 17.6\times10^{-6}$ m, the length of the microbeam to its height is $L^{ref}/h^{ref} = 30$, and the hub radius is $R = 0.1L^{ref}$. The material length scale parameter is considered to be constant for the microbeam equal to $l = 0.2h^{ref}$. The dimensionless rotational velocity is $\hat{\omega}_R = \omega_R\tau$ where $\tau = L^{ref}\sqrt{\frac{I_{0m}}{A_{11m}}}$ in which $A_{11m} = E_m h^{ref}/(1-\nu_m^2)$, and $I_{0m} = \rho_m h^{ref}$. Henceforth, all the above-mentioned values hold for our analyses except when another value for a constant or a parameter is appointed.

Prior to establish some numerical analyses a convergence analysis has been set up. Fig. 3-(a) depicts the critical temperature of a rotating SC X-GPLRC microbeam versus the number of the Ritz terms used in the discretization procedure. The beam rotates at $\hat{\omega}_R = 0.3$. On the other hand, a convergence study for the post-critical response of the observing point of the given rotating beam is presented in Fig. 3-(b). It is deduced that with $N = 9$ the desired precision is achieved.

Here, the influence of simultaneous rotational and thermal loadings on the buckling instability is illustrated. Fig. 4-(a) shows how the critical temperature is affected by means of the slenderness ratio for a stationary SC X-GPLRC microbeam next to a rotating one. It is seen that at a small slenderness ratio, the rotational velocity promotes the buckling strength that predicted for a stationary microbeam. This is as a consequence of the net axial force resulting from the rotational and thermal loadings along the beam span. In contrast by increasing the

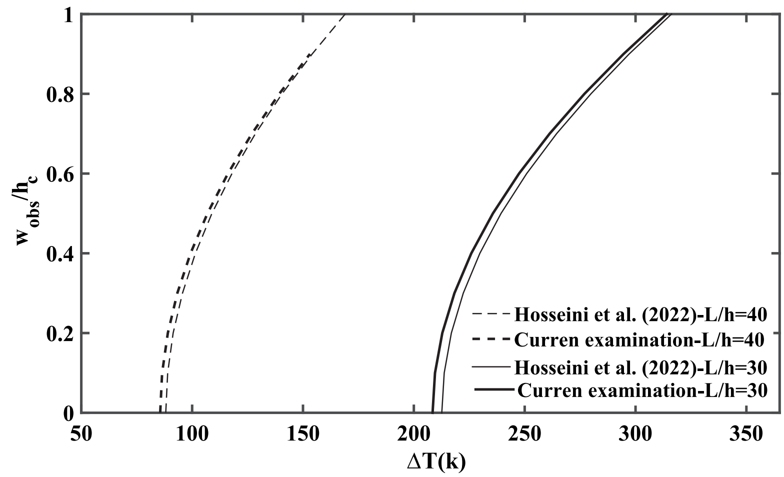

Fig. 2. The post-buckling curves for the mid-point of a rotating CC symmetric sandwich FGM Euler–Bernoulli beam.

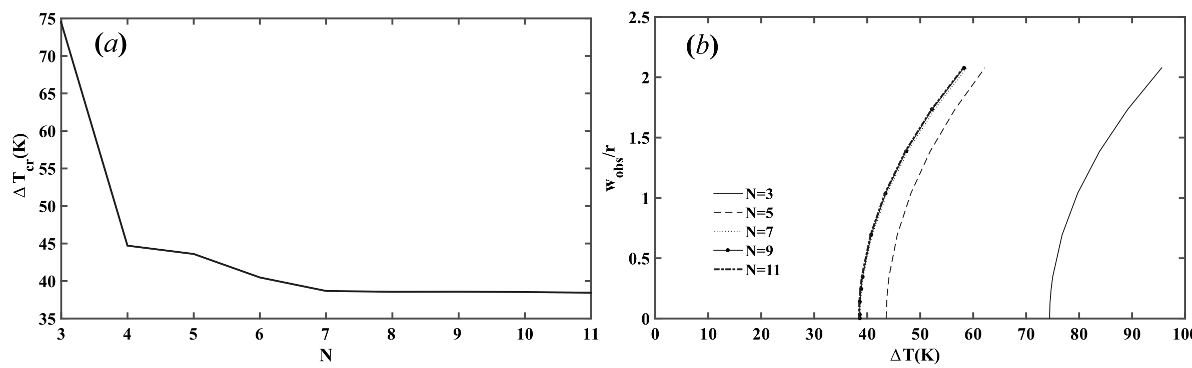

Fig. 3. Convergence examination for (*a*)-the critical temperature, and (*b*)- the post-critical response of the observing point of a rotating SC X-GPLRC beam versus the number the of Ritz terms appointed in the discretization procedure.

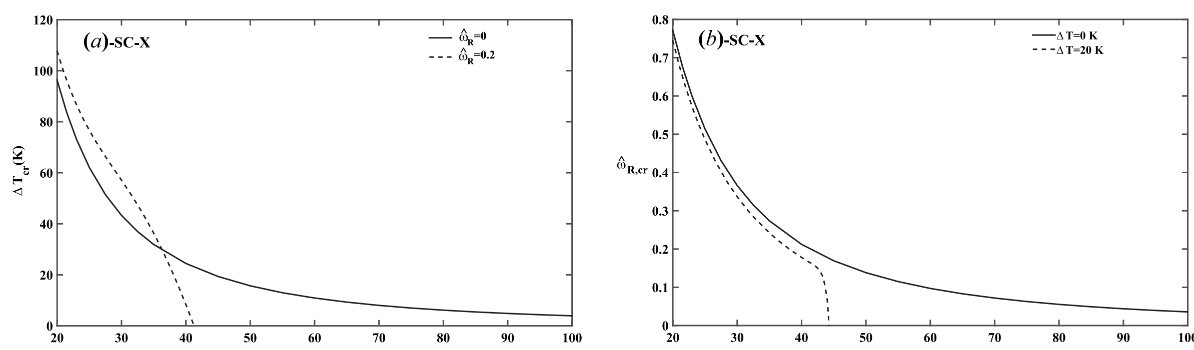

Fig. 4. (*a*)-The critical temperature in terms of the slenderness ratio for a stationary SC X-GPLRC microbeam next to a rotating one, and (*b*)- the critical rotational velocity in terms of the slenderness ratio for a rotating SC X-GPLRC microbeam for pure rotational loading as well as its mutuality with thermal loading.

slenderness ratio, the rotational velocity weakens the aforementioned buckling strength. The implication is that by increasing the slenderness ratio, the net distribution of the axial forces inclines to stretch the rotating beam. Consequently, since the end supports are immovable, the immovability tends to push forward the buckling instability. Another study, i.e. Fig. 4-(*b*) depicts the critical rotational velocity for pure rotational loading as well as its mutuality with thermal loading. It is deduced that operating a rotating beam at a thermal environment reduces the critical slenderness ratio as well as the critical rotating speed sharply.

Fig. 5 renders how the critical temperature of a rotating clamped-simply (CS)/SC X-GPLRC beam varies with in conjunction with the hub radius. It is seen that the critical temperature of a rotating CS X-GPLRC beam is monotically decreasing when the hub radius is increasing. In contrast, for a rotating SC X-GPLRC beam, the critical temperature increases for small rotational speeds ($\hat{\omega}_R < 0.2$); increases then decreases for moderate rotational speeds ($\hat{\omega}_R \cong 0.2$); and decreases monotically for large rotational speeds ($\hat{\omega}_R > 0.2$). As it was mentioned earlier, this is as a consequence of the resulting compressive-stretching axial forces toward the beam span.

The effect of the rotational velocity on the critical temperature of a rotating CS/SC X-/O-GPL microbeam in comparison with a non-reinforced microbeam is illustrated in Fig. 6. The presented results are in regard of the MCST and the classical continuum theory (CCT) when $l/h = 0.0$. It is observed that for zero to moderate rotational velocities adjoining the GPL phase to the matrix reduces the buckling strength,

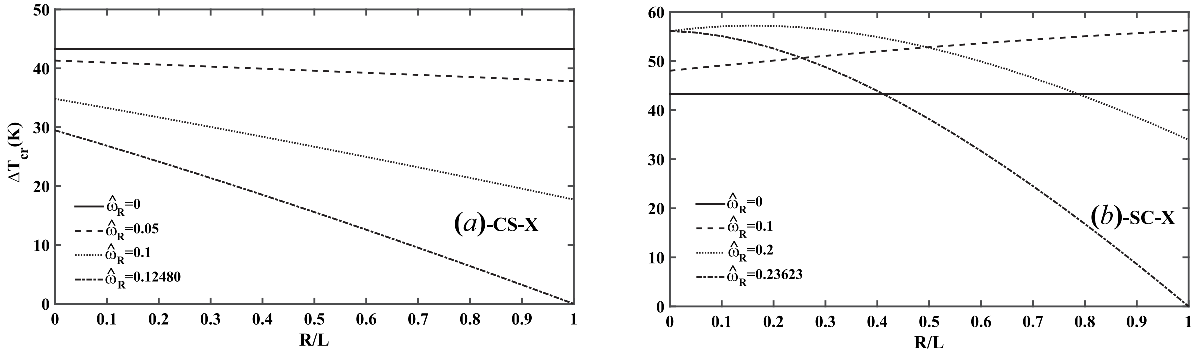

Fig. 5. The critical temperature of a rotating (*a*)-CS, and (*b*)-SC X-GPLRC beam versus the hub radius.

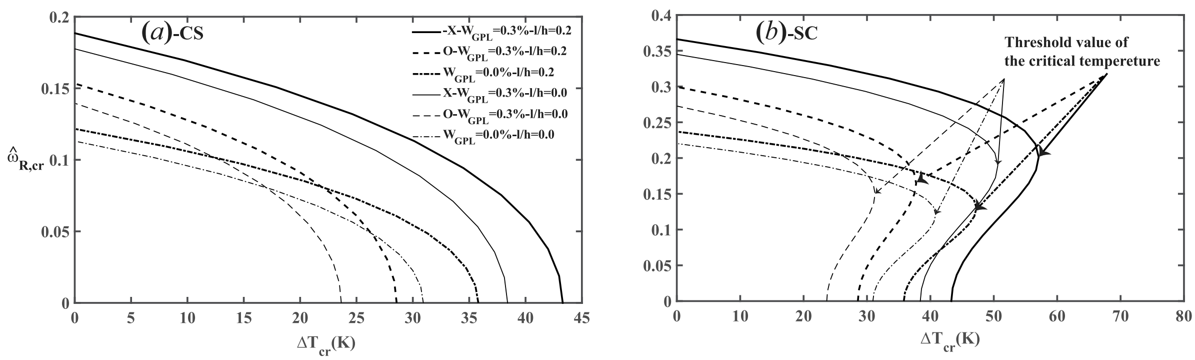

Fig. 6. The relation of the rotational velocity with respect to the critical temperature of a rotating (*a*)-CS, and (*b*)-SC X-/O-GPL microbeam in regard of the MCST and the CCT in comparison with a non-reinforced microbeam.

i.e. the strength of the microbeam against the incidence of the buckling, of a rotating O-GPL microbeam. This is owing to the wide discrepancy between the thermal expansion constants of the matrix phase and the GPL phase. Hence, adding the GPL phase is not recommended at this situation because it diminishes the buckling strength. Moreover, for a rotating SC beam, the buckling temperature increases initially by the decrease of the rotational velocity in an identical trend to a rotating CS beam; however, after reaching a threshold value specified in the figure, it begins to diminish subsequently. This is owing to the mutual distribution of the centrifugal force and the thermal force along the microbeam span when it comes along the support condition. The threshold value of the rotational speed for the assumed data for a rotating SC X/O GPLRC microbeam is $\hat{\omega}_R \cong 0.2$. Accordingly, the threshold value for the rotational speed is the velocity at which the maximum critical temperature arises. Above, and below of the corresponding speed, the critical temperature reduces, sequently, by the increment, and the decrement of the rotational velocity. Furthermore, the results based on regarding the size dependency of the microbeam demonstrates a more stiff structure against the buckling instability.

Fig. 7 shows the impression of the material length scale parameter to the height of the microbeam, i.e. l/h, on the critical temperature of a rotating SC GPLRC microbeam for two different rotational velocities and two various dispersion patterns in comparison with a non-reinforced microbeam. It is implicated that by the decrement of the l/h ratio the critical temperature decreases. In addition, in some circumstances the rotational velocity induces a buckling instability to the rotating microbeam at $T = 300$ K, i.e. without the assistance of any thermal loading. Moreover, with the current data, the rotating SC GPL microbeam with X-pattern does not buckle without the assistance of the temperature increment. Subsequently, it can be inferred that the buckling strength of a microbeam with X-GPL pattern is more than a microbeam with O-GPL pattern. Furthermore, adjoining the GPL phase improves the buckling strength of the rotating microbeam. In addition, at the same conditions, the increment of the rotational velocity decreases the corresponding critical temperature. The last both findings are due to the fact that the two assumed rotational velocities are above the threshold value of the rotating speed for the SC GPLRC microbeam specified in Fig. 6-(*b*), i.e. $\hat{\omega}_R \cong 0.2$.

The impact of the weight fraction of the GPL on the critical temperature of a rotating SC microbeam for three different rotational velocities and two various distribution patterns of GPL is illuminated in Fig. 8. It is deduced that by the decrement of the GPL weight fraction, the critical temperature reduces except for the case that we have applied the threshold value of the rotational speed for a rotating SC O-GPL microbeam, i.e. $\hat{\omega}_R = 0.2$. In this case, by the decrement of the weight fraction of the GPL the critical temperature increases initially but subsequently, it starts to decrease. It is thanks to the reciprocal dispersion of the centrifugal force and the thermal force along the microbeam span when it combines with the support condition. Although we have detected this phenomenon for a rotating O-GPL microbeam, it is observable for a rotating X-GPL microbeam at some rotational velocities.

The impression of the GPL weight fraction on the normalized buckling modeshape, i.e. $\bar{w}$, of a stationary/rotating CS/SC non-reinforced/reinforced X-/O-GPLRC microbeam is presented in Fig. 9. It is seen that although according to Fig. 6 the critical temperature of a stationary CS/SC GPLRC microbeam differs by appending the reinforcement phase as well as the type of the division model of the GPL phase, the associated buckling modeshapes are identical. On the other hand, the buckling modeshape of a rotating GPLRC beam is affected by means of the two aforementioned factors. It is worth mentioning that the buckling modeshape as well as the position of its maximum incidence is impressed more effectively for a rotating SC GPLRC beam relative to a CS one.

Fig. 10 elucidates the impact of the rotational velocity alongside the slenderness ratio on the critical temperature of a rotating CS/SC X-/O-GPL microbeam in accordance with the MCST and the CCT. It is

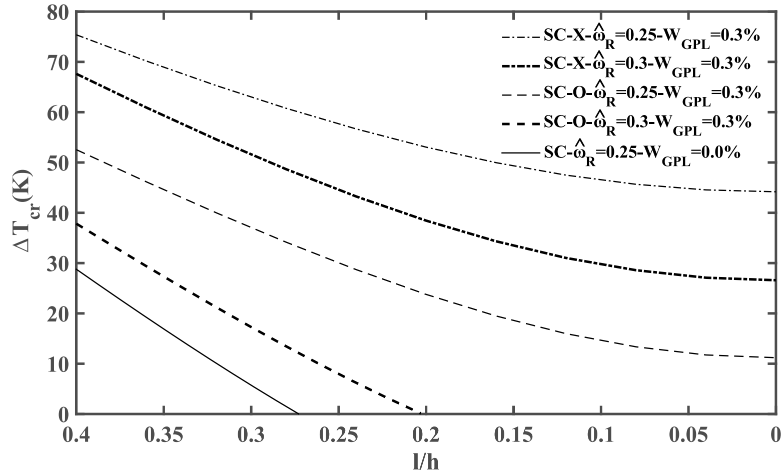

Fig. 7. The relation of the ratio of the material length scale parameter with respect to the height of the microbeam on the critical temperature of a rotating SC X-/O-GPL microbeam for two different rotational velocities in comparison with a non-reinforced microbeam.

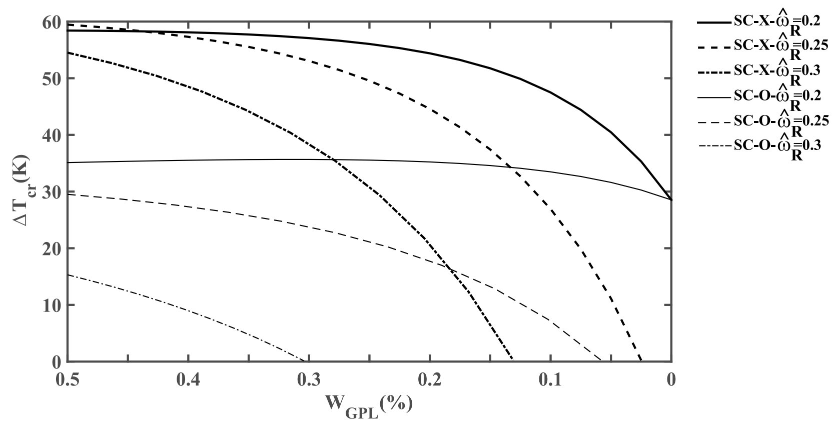

Fig. 8. The relation of the GPL weight fraction with respect to the critical temperature of a rotating SC X-/O-GPL microbeam for three different rotational velocities.

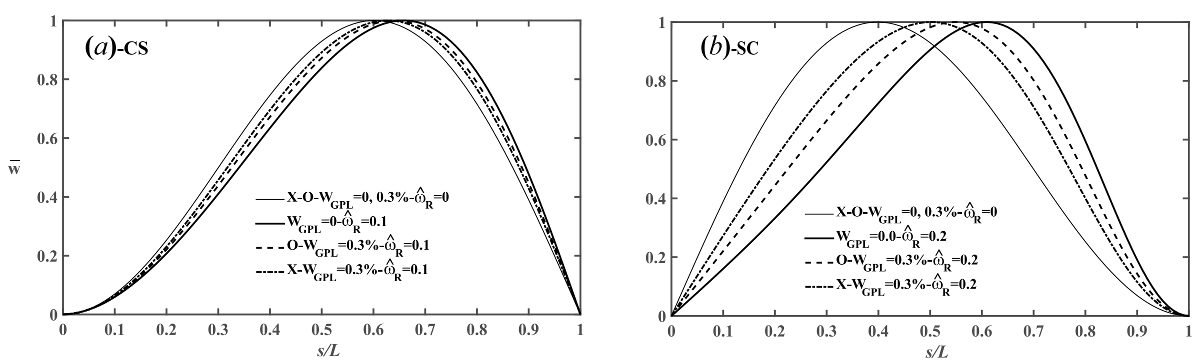

Fig. 9. The impact of the GPL weight fraction on the buckling modeshape of a stationary/rotating CS/SC non-reinforced/reinforced X-/O-GPLRC microbeam.

implicated that by weakening the microbeam as a result of the growth of the slenderness ratio, the critical temperature decreases.

After a comprehensive examination on the thermal buckling instability of a rotating GPL microbeam and studying the influences of the engaged parameters on the critical temperature, with the intention of finding out the impact of the aforementioned parameters on the post-critical deflection some case studies are designed.

The influence of the rotational velocity on the dimensionless post-critical deflection of the observing point, i.e. w_{obs}/r wherein $r = \sqrt{\frac{I}{A}}$ (in which I is the second area moment of inertia about the y-axis and A is the microbeam cross-section) is the radius of gyration, of a rotating CS/SC X-GPL microbeam is depicted in Fig. 11. It is seen that at a similar temperature by the increment of the rotational velocity the observed deflection for the CS microbeam increases. In contrast, for a rotating SC microbeam the associated deflection decreases from zero to the specified threshold value of the rotational velocity while it increases from the specified threshold value to high rotational velocity range. It is seen that the post-critical deflections of a stationary CS and a stationary SC X-GPL microbeams are identical.

Fig. 12 illustrates the influence of the GPL weight fraction on the post-critical deflection for the observing point of a rotating O-GPL CS/SC microbeam for two different rotational velocities. It is shown

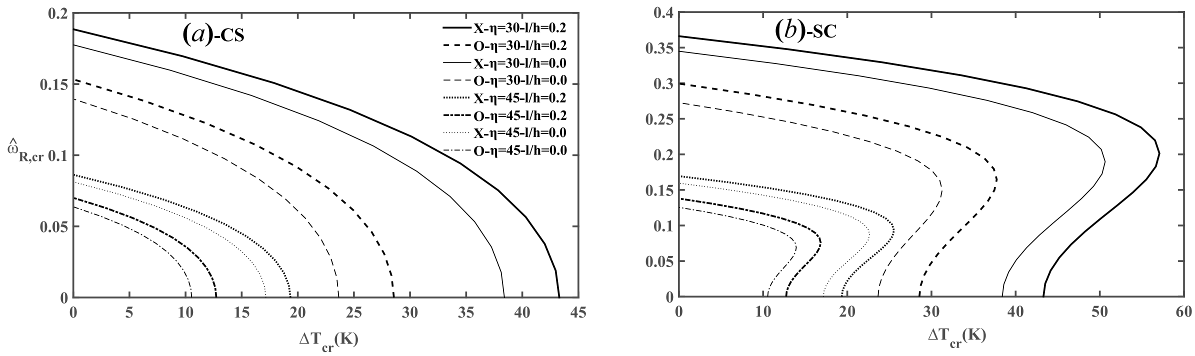

Fig. 10. The impact of the rotational velocity alongside the slenderness ratio on the critical temperature of a rotating (*a*)-CS, and (*b*)-SC X-/O-GPL microbeam in accordance with the MCST and the CCT.

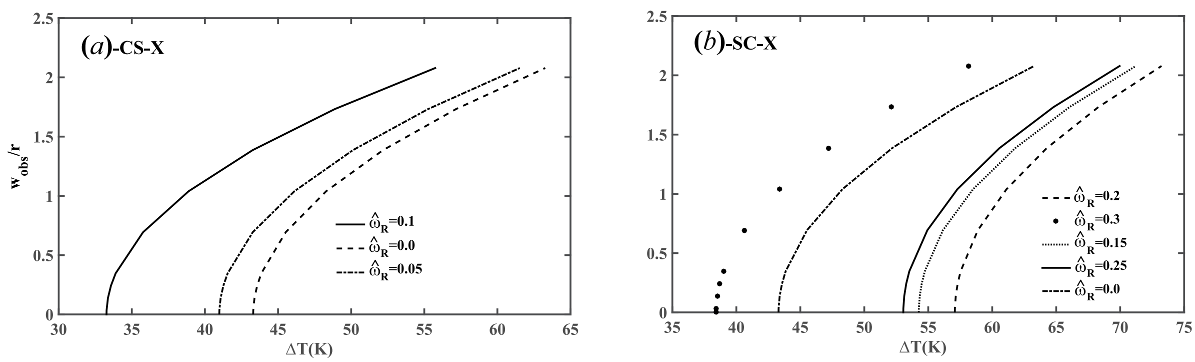

Fig. 11. The influence of the rotational velocity on the post-critical deflection of the observing point of a rotating (*a*)-CS, and (*b*)-SC X-GPL microbeam.

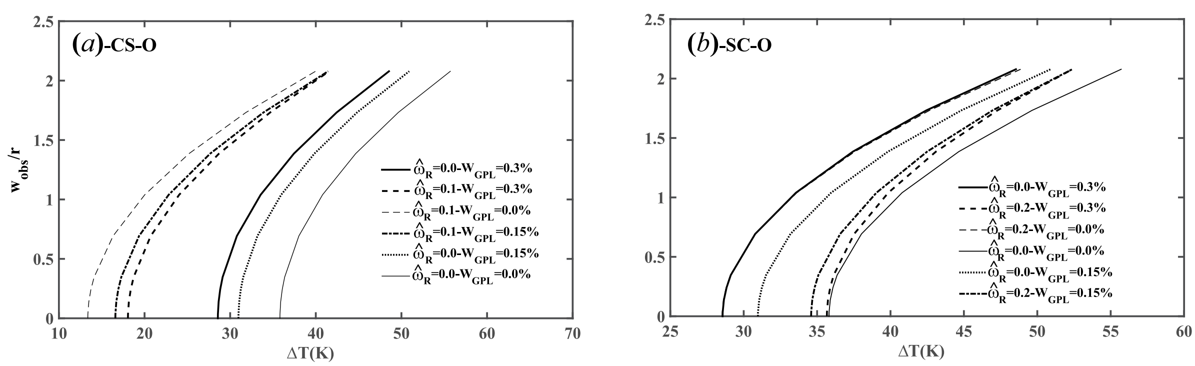

Fig. 12. The influence of the GPL weight fraction on the post-critical deflection for the observing point of (*a*)-a rotating O-GPL CS, and (*b*)-a rotating O-GPL SC microbeams for two different rotational velocities.

that by the increment of the GPL weight fraction at the same temperature the post-critical deflection of a stationary CS/SC microbeam increases while an inverse trend is seen for a rotating CS/SC microbeam. The latter is due to the fact that the considered rotational velocity is beyond the specified threshold value of the rotational speed for a rotating SC GPLRC microbeam, i.e. $\hat{\omega}_R = 0.2$. Moreover, the post-critical deflection for stationary microbeams is more impressed by the GPL weight fraction.

The post-buckling configuration for a rotating CS/SC non-reinforced/reinforced X/O-GPLRC microbeam at different snapshots of the deflection of the observing point has been shown in Fig. 13. It is mentioned earlier that the observing point for the CS, and SC GPLRC microbeam has been situated at the mid-span. Accordingly, the deflection of the mid-span of the provided configurations for the rotating CS/SC non-reinforced/reinforced X/O-GPLRC microbeams at each snapshot is identical. It is seen that in contrast to rotating microbeams, the post-buckling configuration of stationary microbeams is not affected by the GPL division model, and its weight fraction. In addition, the post-buckling configuration of rotating SC GPLRC microbeams is more impressed by the GPL weight fraction as well as its division model.

The effect of the rotational velocity on the post-critical deflection for the observing point of a rotating CS/SC X-GPL microbeam is illustrated in Fig. 14 for three different rotational velocities in the framework of MCST and the CCT. It is deduced that by the increment of the rotational velocity the post-critical deflection of a rotating CS X-GPL microbeam increases at an identical temperature. On the other hand, for the rotating SC X-GPL microbeam that rotates at zero to the specified threshold value for the rotational velocity, the post-critical deflection reduces while on the contrary, it increases for the range of rotational speed between the specified threshold value to high speeds. On the other hand, at the same temperature the MCST predicts a lower deflection relative to the CCT which implies the stiffening impact of the consideration of the length scale parameter.

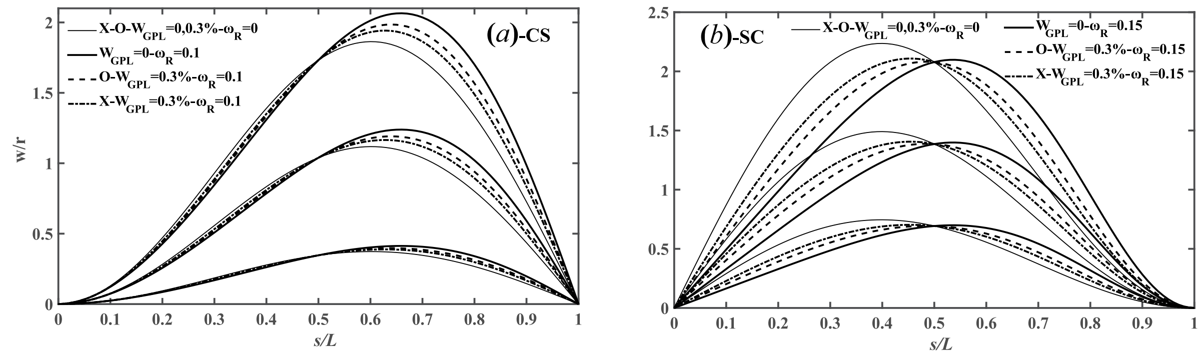

Fig. 13. The post-buckling configuration for (*a*)-a rotating CS, and (*b*)-a rotating SC non-reinforced/reinforced X/O-GPLRC microbeams at different snapshots of the deflection of the observing point.

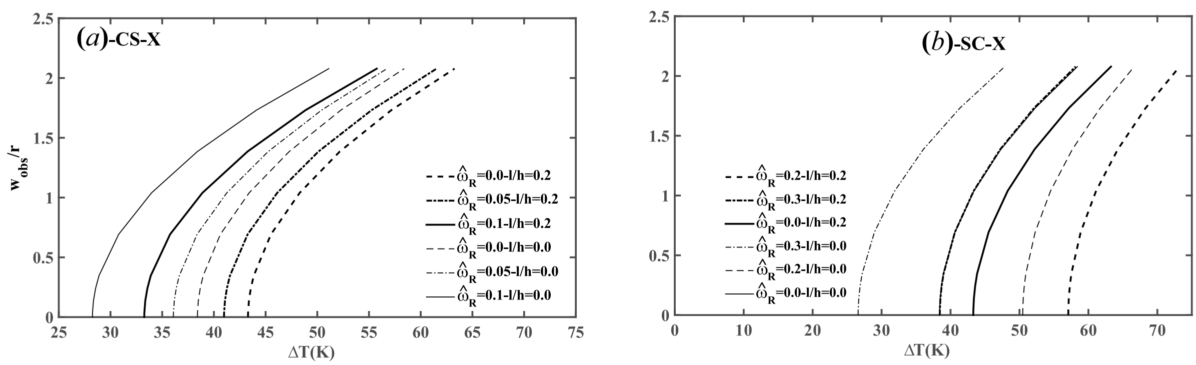

Fig. 14. The effect of the rotational velocity on the post-critical deflection of (*a*)-a rotating CS, and (*b*)-a rotating SC X-GPL microbeams for three different rotational velocities in the framework of MCST and the CCT.

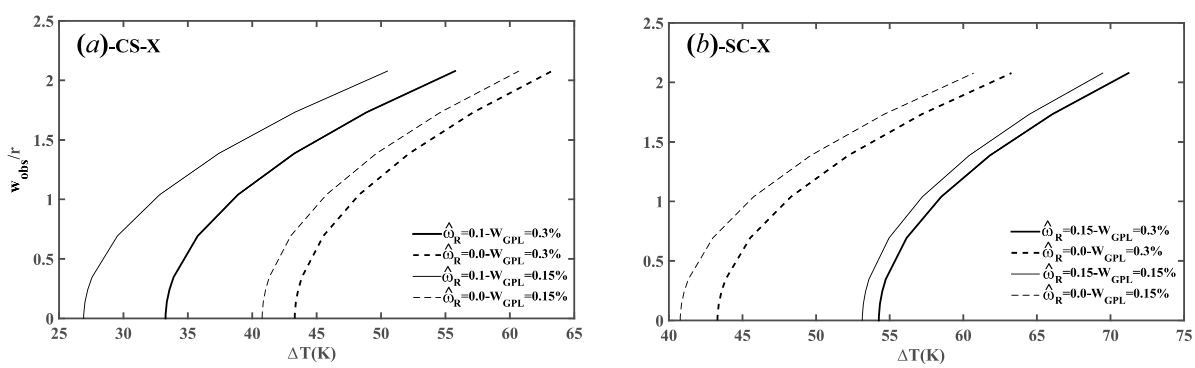

Fig. 15. The impression of the GPL weight fraction on the post-critical deflection of (*a*)-a rotating/stationary CS, and (*b*)-a rotating/stationary SC X-GPL microbeams.

Fig. 15 illuminates the impression of the GPL weight fraction on the post-critical deflection of a rotating/stationary CS/SC X-GPL microbeam. It is inferred that at the same temperature by the increment of the weight fraction of the GPL the post-critical deflection of the observing point of the CS/SC X-GPL microbeam reduces. On the other hand, the GPL weight fraction becomes less effective on the post-critical deflection of rotating GPL microbeams relative to stationary GPL microbeams.

4. Conclusions

In accordance with Halpin–Tsai micromechanical model, the von-Karman strain relation in terms of the displacements, and the MCST hypothesis, the thermal buckling instability and the post-critical deflection of a rotating GPL microbeam were addressed in regard of the Timoshenko beam hypothesis. This research was established for the sake of illuminating the effectiveness of the GPL reinforcement phase on the buckling strength of rotating microbeams in thermal ambient. The Newton–Raphson scheme along with the Ritz procedure delivered the static deformation owing to the centrifugal force induced by the rotation. Some efficient algorithms on the basis of an iterative procedure revealed the buckling temperature and the post-critical deflection of the rotating GPLRC microbeam. The impact of the GPL weight fraction, the GPL distribution pattern, the rotational velocity, and the slenderness ratio on the results were illuminated. It is concluded that:

- At low to a specified threshold value for the rotational velocity range adjoining the GPL phase in the form of an O-GPL pattern reduces the buckling strength of a rotating microbeam.
- For the full range of rotational velocity adjoining the GPL phase in the form of an X-GPL pattern improves the buckling strength of a rotating microbeam.
- Despite a rotating CS microbeam, the trend of the buckling instability temperature and the post-critical deflection of a rotating SC

microbeam depends thoroughly on the rotational velocity value. In other words, we cannot predict qualitatively, the response before a numerical analysis; A numerical analysis that specifies the threshold value of the rotational velocity. The threshold value of the rotational velocity for SC GPLRC microbeams is the speed at which the maximum critical temperature is predicted.

- Increasing the slenderness ratio reduces the buckling temperature of a rotating GPLRC microbeam.
- For a SC GPLRC microbeam as a consequence of increasing the hub radius, the critical buckling temperature increases, increases then diminishes, and reduces, sequently, if the rotating speed is below, about, and above the specified threshold value. However, for a CS one at similar circumstances the critical buckling temperature diminishes.
- At an identical temperature, increasing the rotational velocity, increases the post-critical deflection of a rotating CS GPLRC microbeam.
- At a same temperature, the increment of the rotational velocity, enlarges the post-critical deflection of a rotating SC GPLRC microbeam after an initial decrease.
- By the increment of the temperature, the impact of the GPL weight fraction on the post-critical deflection of a rotating GPLRC microbeam decreases.
- At an identical temperature, the growth of the GPL weight fraction diminishes the post-critical deflection of a rotating CS/SC O-GPL microbeam when the rotational velocity is larger than its threshold value. Moreover, the predicted trend for stationary CS/SC O-GPL microbeams is reverse.
- At a similar temperature, the MCST predicts a lower post-critical deflection relative to the CCT.
- The buckling, and post-buckling modeshapes of stationary GPLRC microbeams is independent of the GPL weight fraction and its scattering pattern. However, they are influenced for rotating GPLRC microbeams. The buckling modeshape and the position of its maximum occurrence for a rotating SC GPLRC microbeam is more affected by the variation of the GPL weight fraction rather than a CS one.

Declaration of competing interest

The authors declare that they have no known competing financial interests or personal relationships that could have appeared to influence the work reported in this paper.

Data availability

No data was used for the research described in the article.

Acknowledgments

The authors extend their appreciation to the Deanship of Scientific Research at King Khalid University, Abha, Saudi Arabia, for funding this work through the Research Group Program under grant no. RGP. 2/19/43. This paper is part of a research project funded by the Office of Research and Sponsored Programs (ORSP), United States at Abu Dhabi University through a research fund (Grant number 19300564).

Appendix

Thermal stress resultants:

$$\{N_{ss}^T, M_{ss}^T\} = \int_{-\frac{1}{2}h}^{\frac{1}{2}h} [Q_{11}(z)\Delta T\alpha(z)\{1, z\}]\mathrm{d}z \tag{34}$$

The longitudinal, longitudinal–flexural, and flexural elastic constants:

$$\{A_{ii}, B_{ii}, D_{ii}\} = \int_{-\frac{1}{2}h}^{\frac{1}{2}h} [Q_{ii}(z)\{1, z, z^2\}]\mathrm{d}z \tag{35}$$

The size-dependent elastic constant:

$$A_{xy} = \int_{-\frac{1}{2}h}^{\frac{1}{2}h} [2G(z)l(z)^2]\mathrm{d}z \tag{36}$$

The inertial constants:

$$\{I_i\} = \int_{-\frac{1}{2}h}^{\frac{1}{2}h} [\rho(z)\{z^i\}]\mathrm{d}z \quad i = 0, 1, 2 \tag{37}$$

References

[1] Zhu P, Lei ZX, Liew KM. Static and free vibration analyses of carbon nanotube-reinforced composite plates using finite element method with first order shear deformation plate theory. Compos Struct 2012;94(4):1450–60.
[2] Ansari R, Shojaei MF, Gholami R, Mohammadi V, Darabi MA. Thermal postbuckling behavior of size-dependent functionally graded Timoshenko microbeams. Int J Non-Linear Mech 2013;50:127–35.
[3] Ebrahimi F, Salari E. Thermal buckling and free vibration analysis of size dependent Timoshenko FG nanobeams in thermal environments. Compos Struct 2015;128:363–80.
[4] Shafiei N, Mousavi A, Ghadiri M. Vibration behavior of a rotating non-uniform FG microbeam based on the modified couple stress theory and GDQEM. Compos Struct 2016;149:157–69.
[5] Ghadiri M, Shafiei N. Vibration analysis of rotating functionally graded Timoshenko microbeam based on modified couple stress theory under different temperature distributions. Acta Astronaut 2016;121:221–40.
[6] Shafiei N, Kazemi M, Ghadiri M. Comparison of modeling of the rotating tapered axially functionally graded Timoshenko and Euler–Bernoulli microbeams. Physica E 2016;83:74–87.
[7] Ilkhani MR, Hosseini-Hashemi SH. Size dependent vibro-buckling of rotating beam based on modified couple stress theory. Compos Struct 2016;143:75–83.
[8] Selim BA, Zhang LW, Liew KM. Vibration analysis of CNT reinforced functionally graded composite plates in a thermal environment based on Reddy's higher-order shear deformation theory. Compos Struct 2016;156:276–90.
[9] Mirjavadi SS, Matin A, Shafiei N, Rabby S, Mohasel Afshari B. Thermal buckling behavior of two-dimensional imperfect functionally graded microscale-tapered porous beam. J Therm Stresses 2017;40(10):1201–14.
[10] Mirjavadi SS, Rabby S, Shafiei N, Afshari BM, Kazemi M. On size-dependent free vibration and thermal buckling of axially functionally graded nanobeams in thermal environment. Appl Phys A 2017;123(5):315.
[11] Sahmani S, Aghdam MM. Axial postbuckling analysis of multilayer functionally graded composite nanoplates reinforced with GPLs based on nonlocal strain gradient theory. The European Physical Journal Plus 2017;132(11):1–17.
[12] Shen HS, Xiang Y, Lin F, Hui D. Buckling and postbuckling of functionally graded graphene-reinforced composite laminated plates in thermal environments. Composites B 2017;119:67–78.
[13] Wu H, Yang J, Kitipornchai S. Dynamic instability of functionally graded multilayer graphene nanocomposite beams in thermal environment. Compos Struct 2017;162:244–54.
[14] Shenas A Ghorbani, Malekzadeh P, Ziaee S. Thermal buckling of rotating pre-twisted functionally graded microbeams with temperature-dependent material properties. Acta Mech 2017;228(3):1115–33.
[15] Shenas AG, Ziaee S, Malekzadeh P. Post-buckling and vibration of post-buckled rotating pre-twisted FG microbeams in thermal environment. Thin-Walled Struct 2019;138:335–60.
[16] Yang J, Chen D, Kitipornchai S. Buckling and free vibration analyses of functionally graded graphene reinforced porous nanocomposite plates based on Chebyshev-Ritz method. Compos Struct 2018;193:281–94.
[17] Zhong R, Wang Q, Tang J, Shuai C, Qin B. Vibration analysis of functionally graded carbon nanotube reinforced composites (FG-CNTRC) circular, annular and sector plates. Compos Struct 2018;194:49–67.
[18] Lin HG, Cao DQ, Xu YQ. Vibration, buckling and aeroelastic analyses of functionally graded multilayer graphene-nanoplatelets-reinforced composite plates embedded in piezoelectric layers. Int J Appl Mech 2018;10(03):1850023.
[19] Eyvazian A, Taghizadeh SA, Hamouda AM, Tarlochan F, Moeinifard M, Gobbi M. Buckling and crushing behavior of foam-core hybrid composite sandwich columns under quasi-static edgewise compression. J Sandw Struct Mater 2021;23(7):2643–70.
[20] Eyvazian A, Hamouda AM, Tarlochan F, Mohsenizadeh S, Dastjerdi AA. Damping and vibration response of viscoelastic smart sandwich plate reinforced with non-uniform Graphene platelet with magnetorheological fluid core. Steel Compos Struct 2019;33(6):891–906.
[21] Mao JJ, Zhang W. Buckling and post-buckling analyses of functionally graded graphene reinforced piezoelectric plate subjected to electric potential and axial forces. Compos Struct 2019;216:392–405.
[22] Eyvazian A, Shahsavari D, Karami B. On the dynamic of graphene reinforced nanocomposite cylindrical shells subjected to a moving harmonic load. Internat J Engrg Sci 2020;154:103339.

[23] Zhao X, Chen B, Li YH, Zhu WD, Nkiegaing FJ, Shao YB. Forced vibration analysis of Timoshenko double-beam system under compressive axial load by means of Green's functions. J Sound Vib 2020;464:115001.
[24] Zhao X, Zhu WD, Li YH. Analytical solutions of nonlocal coupled thermoelastic forced vibrations of micro-/nano-beams by means of Green's functions. J Sound Vib 2020;481:115407.
[25] Arvin H. On parametrically excited vibration and stability of beams with varying rotating speed. Iran J Sci Technol Trans Mech Eng 2019;43(2):177–85.
[26] Khosravi S, Arvin H, Kiani Y. Interactive thermal and inertial buckling of rotating temperature-dependent FG-CNT reinforced composite beams. Composites B 2019;175:107178.
[27] Khosravi S, Arvin H, Kiani Y. Vibration analysis of rotating composite beams reinforced with carbon nanotubes in thermal environment. Int J Mech Sci 2019;164:105187.
[28] Hosseini SMH, Arvin H. Thermo-rotational buckling and post-buckling analyses of rotating functionally graded microbeams. Int J Mech Mater Des 2021;17(1):55–72.
[29] Hosseini SMH, Arvin H. Free vibration analysis of pre/post-buckled rotating functionally graded sandwich micro-beams. Microsyst Technol 2021;27(5):2049–61.
[30] Xu X, Zhang C, Khan A, Sebaey TA, Farouk N. Instability and post-instability examination due to the buckling of rotating nanocomposite beams in thermal ambient. Int J Mech Mater Des 2022;18(1):87–103.
[31] Reddy JN. Mechanics of laminated composite plates and shells: theory and analysis. CRC Press; 2003.
[32] Meirovitch L. Principles and techniques of vibrations. vol. 1, Upper Saddle River, NJ: Prentice Hall; 1997.
[33] Reddy JN. An introduction to nonlinear finite element analysis second edition: with applications to heat transfer, fluid mechanics, and solid mechanics. OUP Oxford; 2014.
[34] Mason JC, Handscomb DC. Chebyshev polynomials. CRC Press; 2002.
[35] Kiani Y. Free vibration of functionally graded carbon nanotube reinforced composite plates integrated with piezoelectric layers. Comput Math Appl 2016;72(9):2433–49.
[36] Komijani M, Esfahani SE, Reddy JN, Liu YP, Eslami MR. Nonlinear thermal stability and vibration of pre/post-buckled temperature-and microstructure-dependent functionally graded beams resting on elastic foundation. Compos Struct 2014;112:292–307.
[37] Hosseini SMH, Arvin H, Kiani Y. On buckling and post-buckling of rotating clamped-clamped functionally graded beams in thermal environment. Mech Based Des Struct Mach 2022;50(8):2779–94.